



Equivalence of three thermal boundary conditions in compressible turbulent channel flows

Peng Zhang (张朋) ¹, Yubin Song (宋余滨)¹, Yilang Liu (刘溢浪)¹, and Zhenhua Xia (夏振华) ^{1,2,*}

¹State Key Laboratory of Fluid Power and Mechatronic Systems, and Department of Engineering Mechanics, Zhejiang University, Hangzhou 310027, China

²Guangdong Provincial Key Laboratory of Turbulence Research and Applications, Southern University of Science and Technology, Shenzhen 518055, China



(Received 10 March 2022; accepted 31 May 2022; published 16 June 2022)

In this paper, direct numerical simulations have been performed to explore the equivalence of different thermal boundary conditions in compressible turbulent channel flows at fixed $Re = 6000$, $Ma = 1.5$. Three canonical types of thermal boundary conditions will be investigated at almost equivalent setups, including the first boundary condition with fixed wall temperature T_w (constant Dirichlet boundary condition), the second boundary condition with fixed wall heat-flux q_w (constant Neumann boundary condition), and the third boundary condition (Robin boundary condition). The turbulent statistics of the temperature and velocity fields, including mean profiles, root-mean-square values, second-order statistics, and normalized probability density functions, temperature stripes near the wall and the budget of internal energy have been analyzed in detail to clarify the differences caused by the different thermal boundary conditions. The results show that the three thermal boundary conditions have almost negligible effect on the velocity field, whereas some discernible deviations can be observed for the temperature field in the near-wall region with $y^+ \lesssim 30$. Furthermore, the statistics from the second and third thermal boundary conditions are very close, enabling the usage of the second boundary condition to mimic the more complex third boundary conditions.

DOI: [10.1103/PhysRevE.105.065106](https://doi.org/10.1103/PhysRevE.105.065106)

I. INTRODUCTION

Compressible wall-bounded turbulence is of great importance in many engineering applications, such as the supersonic and hypersonic vehicles. Different from the incompressible wall-bounded turbulence, the wall-temperature condition becomes one of the crucial features in compressible wall-bounded turbulence. For example, the wall temperature on the surface of the supersonic vehicles is essentially adiabatic, whereas it is significantly lower than the adiabatic wall temperature in hypersonic vehicles due to the substantial radiative cooling and internal heat transfer [1].

Thanks to the pioneering works from Coleman and co-workers [2,3], direct numerical simulations (DNSs) have been becoming one of the powerful tools to investigate the compressible wall-bounded turbulence. In the implementations of the DNSs, different wall-temperature boundary conditions were adopted, either the first thermal boundary condition also denoted as the Dirichlet boundary condition where the wall-temperature T_w was prescribed with a constant value (isothermal) [2,4–11],

$$T_w = c_1, \quad (1)$$

or the second thermal boundary condition also denoted as the Neumann boundary condition where the wall heat-flux q_w was

specified with a constant value (isoflux),

$$q_w = -\lambda \left. \frac{dT}{dn} \right|_w = c_2. \quad (2)$$

Here, λ is the thermal conductivity coefficient, n is the normal direction of the wall, and the constant c_2 is usually zero to mimic the adiabatic wall-boundary condition [4–6,11–13]. It should be noted that in many numerical simulations of compressible turbulent boundary layer flows, the adiabatic wall-boundary condition was not implemented directly but substituted with the isothermal wall-temperature instead where the wall temperature was set equal to the adiabatic temperature with the constant recovery factor (or the recovery temperature) [1,14–17]. The underlying philosophy of such substitution, which is also called the pseudoadiabatic [13], is that the isothermal adiabatic wall-temperature can mimic the adiabatic thermal boundary condition in simulation of compressible wall-bounded turbulence. Recent DNS results of supersonic turbulent boundary layer by Shadloo *et al.* [6] confirmed that basic turbulent statistics were not affected by above substitution for adiabatic boundary except for some deviations of the near-wall asymptotic behaviors.

In many real-life problems, especially for those cases when the thermal diffusivity of the fluid and the solid are of the same order of magnitude, the thermal interaction between the solid wall, and the fluid must be considered. However, for these problems, neither the isothermal nor the isoflux boundary conditions could mimic the actual heat transfer behavior realistically, and new treatments on the thermal boundary

*xiazh@zju.edu.cn

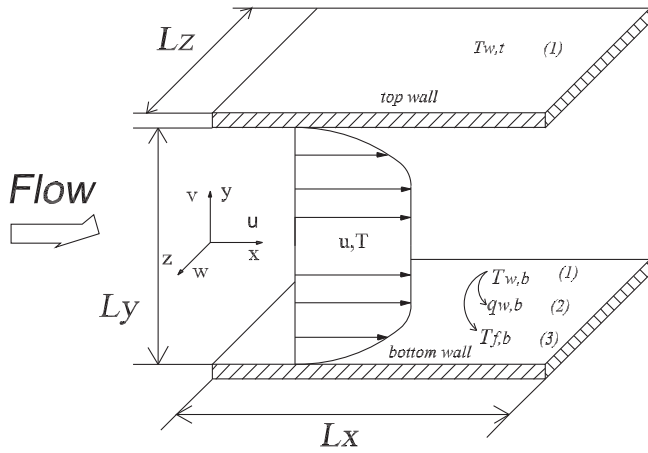


FIG. 1. Schematic of a compressible turbulent channel flow. On the top wall, the isothermal boundary condition is applied. On the bottom wall, three different thermal boundary conditions, i.e., (1)–(3), are applied in three cases at almost equivalent setups.

condition should be adopted. A natural choice is to consider the thermal conductivity in the solid wall together with the thermal diffusivity in the fluid, i.e., the conjugate heat transfer. Tiselj *et al.* [18] once investigated the influence of the thermal boundary conditions in incompressible turbulent channel flows with passive scalar transfer by DNS. They performed direct comparisons among the conjugate heat transfer, the imposed temperature and the imposed heat flux at the wall, and observed substantial temperature fluctuations in the near-wall region for the cases with conjugate heat transfer and the isoflux boundary conditions. Another simplified option is to use the Robin boundary condition, where

$$h_0 T_w + \lambda \left. \frac{\partial T}{\partial n} \right|_w = C. \quad (3)$$

Here, h_0 is the heat transfer coefficient. The above Eq. (3) could be rewritten in the following form, equivalently,

$$-\lambda \left. \frac{dT}{dn} \right|_w = h_0 (T_f - T_w), \quad (4)$$

with $T_f = 2T_w - C/h_0$ denoting the temperature of the external fluid surrounding the object boundary [19]. In fact, in the implementation of the conjugate heat transfer boundary condition for temperature, which was a passive scalar, Tiselj *et al.* [18] indeed used the Robin boundary condition for the fluid side of the fluid-solid boundary and reported that the influence of the thermal boundary condition was within a couple of wall units depending on the Prandtl number Pr . The influence range of the temperature boundary conditions is $y^+ \approx 15$ for $Pr = 0.71$ and $y^+ \approx 6-8$ for $Pr = 5-7$, respectively. Flageul *et al.* [20] also carried out an investigation on the effect of four different thermal boundary conditions, including the Dirichlet, Neumann, Robin, and the conjugate heat transfer boundary conditions, through DNS for incompressible turbulent channel flows with passive scalar, and they also found that the temperature variance was strongly impacted in the near-wall region by the different thermal boundary conditions,

and that the several statistics from the Robin boundary condition were almost the same as those from the conjugated case. They also concluded that their results enabled a simplified Robin boundary condition to mimic a clearly more complex conjugated condition involving a fluid-solid thermal interaction. Other studies on the effects of different thermal boundary conditions in incompressible or low Mach-number wall-bounded flows with passive scalar transport include but are not limited to Refs. [18,20–31].

Compared to the numerous papers on the incompressible or low Mach-number wall-bounded flows, very few works have been devoted to study the effect of thermal boundary conditions in compressible wall-bounded turbulence, although the temperature field is coupled with the velocity field in compressible flows, making the thermal boundary conditions more critical for the results. Morinishi *et al.* [4] once investigated the effects of adiabatic and isothermal conditions on the statistics in compressible turbulent channel flows. In their studies, they performed DNS on turbulent channel flows with adiabatic and isothermal walls where one side was set to the physical adiabatic condition and the other was isothermal. Their results showed that Morkovin's hypothesis was not applicable to the near-wall asymptotic behavior of the wall-normal turbulence intensity, even if the variable property effect was considered. Later on, Tamano and Morinishi [5] performed a direct comparison between the adiabatic wall and an equivalent isothermal wall in compressible turbulent channel flows, and they reported that the substitution of adiabatic wall with an equivalent isothermal wall led to obvious difference in the mean temperature profiles at the high-temperature and adiabatic walls where an additional maximum of the mean temperature and the corresponding maximum of root-mean-square (rms) temperature fluctuations existed near the high-temperature wall. This observation conflicts with the recent results drawn by Shadloo *et al.* [6] in supersonic boundary layers where the basic turbulent statistics were not affected by the thermal boundary conditions. The biggest conflict is whether the different thermal boundary conditions can affect the statistics away from the wall. The results of Tamano and Morinishi [5] supported this argument, whereas those from Shadloo *et al.* [6] disapproved. According to the mean temperature profile [See Fig. 2(a) in Tamano and Morinishi [5]], the wall temperature at the upper wall in case 1 was somehow lower than required, and we inferred that the upper wall was, in fact, nonadiabatic.

In the present paper, DNSs of compressible turbulent channel flows are performed to investigate the effect of different thermal boundary conditions on turbulent statistics and flow structures in detail. Three canonical thermal boundary conditions, including the Dirichlet, Neumann, and Robin boundary conditions were adopted at almost equivalent setups. Our aim is to provide direct numerical evidences not only on the effect of different thermal boundary conditions on compressible wall-bounded turbulence, which can be used to improve the Reynolds averaged Navier-Stokes and large eddy simulation modeling [32], but also on the equivalence of the three thermal boundary conditions, which can resolve the above conflicting observations between Tamano and Morinishi [5] and Shadloo *et al.* [6].

TABLE I. Details of the thermal boundary conditions at the three cases. Here, the values with bold form and underline denote the input values, whereas the other ones are the calculated mean values at the statistically stationary state. The friction Reynolds number $Re_\tau = \rho_w u_\tau h / \mu_w$ is defined using the quantities at the wall. The heat transfer coefficient is kept the same at all three cases when $T_{f,b}$ is estimated. The rms values of q_w , T_w , and T_f are calculated in the bottom wall for all cases.

Case	$Re_{\tau,b}$	$T_{w,b}$	$q_{w,b}$	$T_{f,b}$	$T_{w,b,rms}/\langle T_{ref} \rangle$	$q_{w,b,rms}/\langle q_w \rangle$	$T_{f,b,rms}/\langle T_{f,b} \rangle$	$Re_{\tau,t}$	$T_{w,t}$
M15T11	407.8	<u>1.000</u>	-3.407×10^{-3}	-4.105	0	0.4050	0.5037	407.2	<u>1.000</u>
M15T21	413.2	0.985	<u>-3.407×10^{-3}</u>	-4.106	0.131	0	0.0315	406.7	<u>1.000</u>
M15T31	409.9	0.991	-3.401×10^{-3}	<u>-4.105</u>	0.118	0.0230	0	405.5	<u>1.000</u>

II. NUMERICAL SETUP

A. Governing equations

In the present paper, the three-dimensional compressible turbulent flow with the perfect gas assumption is considered, and the flow can be described by the following governing equations:

$$\frac{\partial \rho}{\partial t} + \frac{\partial \rho u_j}{\partial x_j} = 0, \quad (5)$$

$$\frac{\partial \rho u_i}{\partial t} + \frac{\partial (\rho u_i u_j + p \delta_{ij})}{\partial x_j} = \frac{\partial \tau_{ij}}{\partial x_j} + f_i \delta_{i1}, \quad (6)$$

$$\frac{\partial E}{\partial t} + \frac{\partial (E + p) u_i}{\partial x_i} = \frac{\partial u_i \tau_{ij}}{\partial x_j} - \frac{\partial q_i}{\partial x_i} + f_i u_i. \quad (7)$$

Here, the Einstein summation convention and notations are used. δ_{ij} is the Kronecker tensor, ρ is the density, u_i is velocity, p is the pressure, f_i is volume force, and $E = \rho(e + u_i^2/2)$ is the total energy with e being the internal energy. The equation of state is $p = \rho RT$ with R as the gas constant. $e = c_v T$ with $c_v = R/(\gamma - 1)$, and c_p being the specific heat at constant volume and constant pressure, respectively. $\gamma = c_p/c_v = 1.4$ is the specific heat ratio. The shear stress τ_{ij} and heat-flux q_j can be defined as

$$\tau_{ij} = \mu \left(\frac{\partial u_i}{\partial x_j} + \frac{\partial u_j}{\partial x_i} \right) - \frac{2}{3} \mu \frac{\partial u_k}{\partial x_k} \delta_{ij}, \quad q_i = -\lambda \frac{\partial T}{\partial x_i},$$

where the dynamic viscosity μ follows Sutherland's formula [33], and the thermal conductivity λ is estimated through the fixed Prandtl number $Pr = c_p \mu / \lambda = 0.72$.

B. Numerical settings

A sketch of a three-dimensional fully developed compressible turbulent channel flows with three different thermal boundary conditions is shown in Fig. 1. The DNS is carried out in a cuboid box whose sizes in the streamwise (x), wall-normal (y), and spanwise (z) directions are L_x , L_y , and L_z , respectively. The periodic boundary condition is applied in the x and z directions for both the velocity and the temperature fields. In the wall-normal direction, the boundary conditions are different for the velocity and temperature fields. For the velocity field, the no-slip condition is employed, i.e., $u = v = w = 0$ at both walls. For the temperature field, the isothermal Dirichlet boundary condition with $T = T_{w,t}$ is applied at the top wall whereas three different boundary conditions are adopted at the bottom wall, including the Dirichlet boundary condition with $T = T_{w,b} = T_{w,t}$ for the case of M15T11, the Neumann boundary condition with fixed $q_{w,b}$ for the case of M15T21, and the Robin boundary condition with prescribed

$T_{f,b}$ for the case of M15T31 as listed in Table I. It should be noted that $q_{w,b}$ in case M15T21 and $T_{f,b}$ in case M15T31 are prescribed based on the values estimated from case M15T11. Therefore, the three cases are at almost equivalent setups. The well-validated high-order finite difference code OPENCDF [34–38] is used in the present simulations where the inviscid and viscous terms are discretized using a seventh-order upwind scheme and an eighth-order central scheme, respectively, and the time is advanced using an explicit third-order Runge-Kutta scheme.

In the simulations, all quantities are nondimensionalized by a reference temperature $T_{ref} = 288.15$ K, the channel half-width h , the bulk-averaged density $\rho_m = \int_{-h}^h \bar{\rho} dy / (2h)$, and the bulk velocity $u_m = \int_{-h}^h \bar{u} dy / (2h \rho_m)$. Here, $\bar{\phi}$ (or $\langle \phi \rangle$) denotes the averaging operation in x , z , and t for a quantity ϕ . The Reynolds number Re and the Mach number Ma are defined as

$$Re = \frac{\rho_m u_m h}{\mu_{ref}}, \quad Ma = \frac{u_m}{c_0},$$

with the dynamic viscosity μ_{ref} and the sound speed c_0 are the values at T_{ref} . In all cases, $Re = 6000$ and $Ma = 1.5$ remain unchanged, and the computational domain is $L_x \times L_y \times L_z = 4\pi \times 2 \times 4\pi/3$. The grid point is uniform in the x and z directions with $N_x \times N_z = 400 \times 320$, which corresponds to a grid resolution with $\Delta x^+ \times \Delta z^+ \approx 12.8 \times 5.3$, whereas it is clustered in the near-wall region in the y direction with $\Delta y^+ \in [0.6, 10.6]$. Here, the superscript $+$ denotes the normalization by the viscous length scale $\delta_v = \mu_w / (\rho_w u_\tau)$ and friction velocity $u_\tau = (\tau_w / \rho_w)^{1/2}$, for example, $y^+ = y / \delta_v$, $u_{rms}^+ = u_{rms} / u_\tau$. Here, τ_w is the wall shear stress, respectively. The present grid resolution is fine enough and comparable with those used by Modesti and Pirozzoli [9] and Li *et al.* [39]. It is worth noting that the case of M15T11 is actually from Zhang and Xia [38] where the reliability of the code and the grid resolution have been well documented. Meanwhile, the time step is $0.001h/u_m$, and the flow statistics are averaged over 300 samples with an interval $0.8h/u_m$ when the simulations reach the stationary states. In the simulations, M15T11 was first carried out with an initial field where the velocity is the laminar profile plus random disturbances, and the temperature is uniform. The simulation takes more than $300h/u_m$ to reach its stationary state. After we obtained the statistics in M15T11, Cases M15T21 and M15T31 were then carried out, starting from one instantaneous field at the stationary state from M15T11 with the prescribed $q_{w,b}$ and $T_{f,b}$, respectively, at the bottom wall. The corresponding transient time period is around $200h/u_m$.

In the following investigations, the Reynolds decomposition ($\phi = \bar{\phi} + \phi'$, $\bar{\phi} = \langle \phi \rangle$) and Favre decomposition ($\phi = \bar{\phi} + \phi''$, $\bar{\phi} = \overline{\rho\phi}/\bar{\rho}$, $\tilde{\phi} = \{\phi\}$) will be used. The rms value is defined as $\phi_{\text{rms}} = \sqrt{\overline{\phi'^2}}$.

III. RESULTS AND DISCUSSIONS

A. Basic statistics on the velocity and temperature fields

Figure 2 shows the profiles of the mean streamwise velocity, mean temperature, and mean density from the three cases with different thermal boundary conditions at the bottom wall. It is easy to see that the mean streamwise velocity profiles from the three cases coincide with each other across the whole channel, whereas some small deviations are observed among the three cases for the mean temperature profiles. In the bulk region where $-0.9 \lesssim y \lesssim 0.9$, $\langle T \rangle$ from the cases M15T21 and M15T31 are almost the same, exhibiting a slight asymmetry, and their values are around 1% lower than those from the reference case of M15T11. Furthermore, as can be seen from Fig. 2(b) and Table I, the mean temperature on the bottom wall show slight difference, and around 1.5% and 1.0% reductions as compared to $T_{w,b}$ from the reference case of M15T11, can be observed for cases M15T21 and M15T31, respectively. The present results for compressible flows are consistent with those results obtained from the incompressible channel flow with passive scalar transport where the passive scalar should not affect the velocity field and Tiselj *et al.* [23] observed well-matched mean temperature profiles with the differences being less than 1% for the cases with constant T_w and constant q_w . It should be noted that there was another constraint for the constant heat-flux boundary condition in Tiselj *et al.* [23], i.e., the time and space averaged dimensionless wall temperature was fixed to zero, which may eliminate the differences of the mean-wall temperature. For the mean density profiles from different cases as shown in Fig. 2(c), no obvious difference is observed in the bulk region except in the near-wall region with $y^+ \leq 10$.

Figures 3 and 4 show the distributions of the rms values of the velocity and temperature fields, respectively, in the bottom and top half of the channel. It is seen from Figs. 3(b) and 4(b) that there is no discernible divergences among the three cases for both the velocity and temperature fields at the top half of the channel, which is consistent with the fact that the thermal boundary condition is the same on the top wall for the three cases. However, at the bottom half of the channel, different thermal boundary conditions will result in different statistics. For the velocity field as shown in Fig. 3(a), some small difference between the case of M15T11 and the case of M15T21 are observed within $y^+ \lesssim 10$ for the streamwise component, and some tiny divergences between M15T11 and M15T21 can be observed around $y^+ = 50$ for the spanwise component and the wall-normal component. However, the differences between M15T21 and M15T31 are almost indiscernible for all three components. Considering the facts that the temperature can alter the density and the viscosity in the governing equations for velocity and that the only production term in the budget equations of the Reynolds normal stresses [40] explicitly includes the density and viscosity, the difference of u_{rms} among the three cases near the bottom wall may

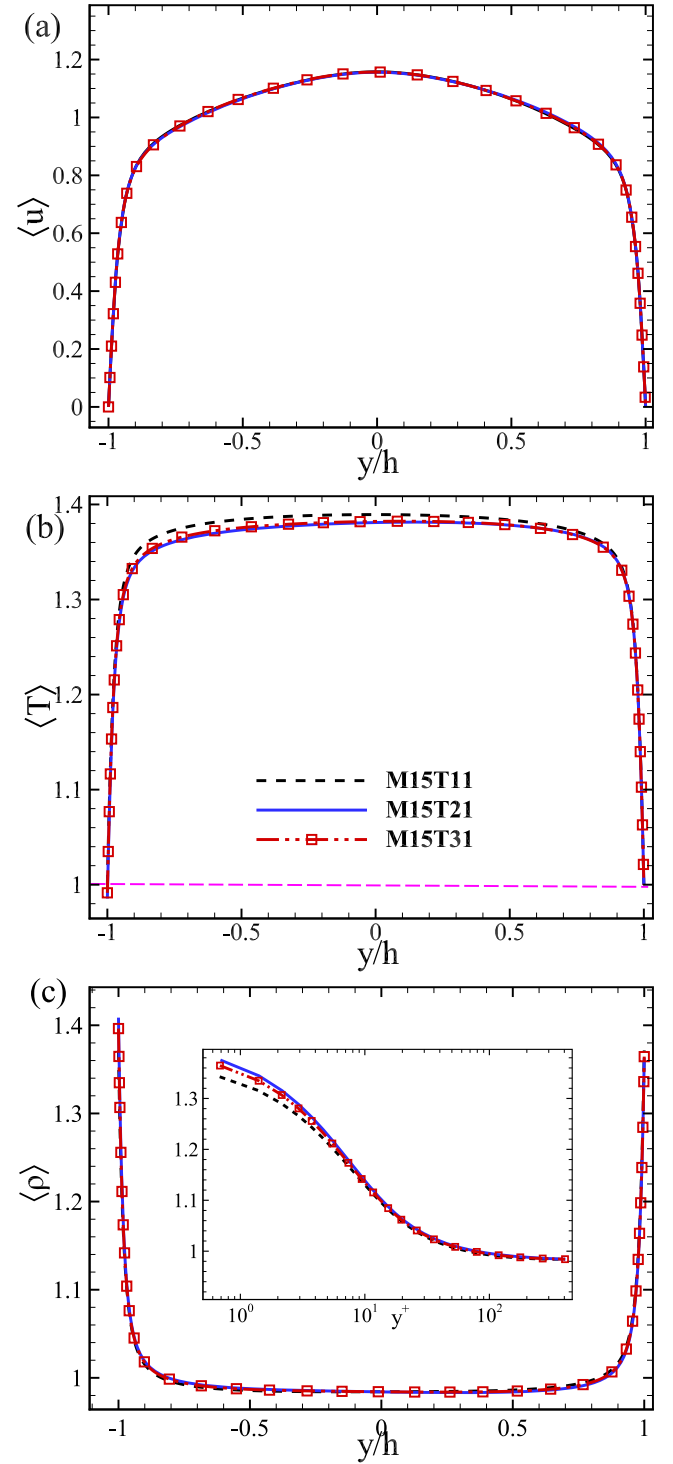


FIG. 2. Profiles of (a) mean streamwise velocity (normalized by u_m), (b) mean temperature (normalized by T_{ref}), and (c) mean density (normalized by ρ_m) in global coordinate (normalized by h). The inset in (c) shows the corresponding near-wall behavior.

be attributed to the different density [see the mean density in the near-wall region shown in Fig. 2(c)] and viscosity. This situation is in sharp contrast to the incompressible case where the velocity field could not be modified by the passive scalar. For the temperature fluctuations near the bottom wall, clear divergence could be observed as shown in Fig. 4(a). For the

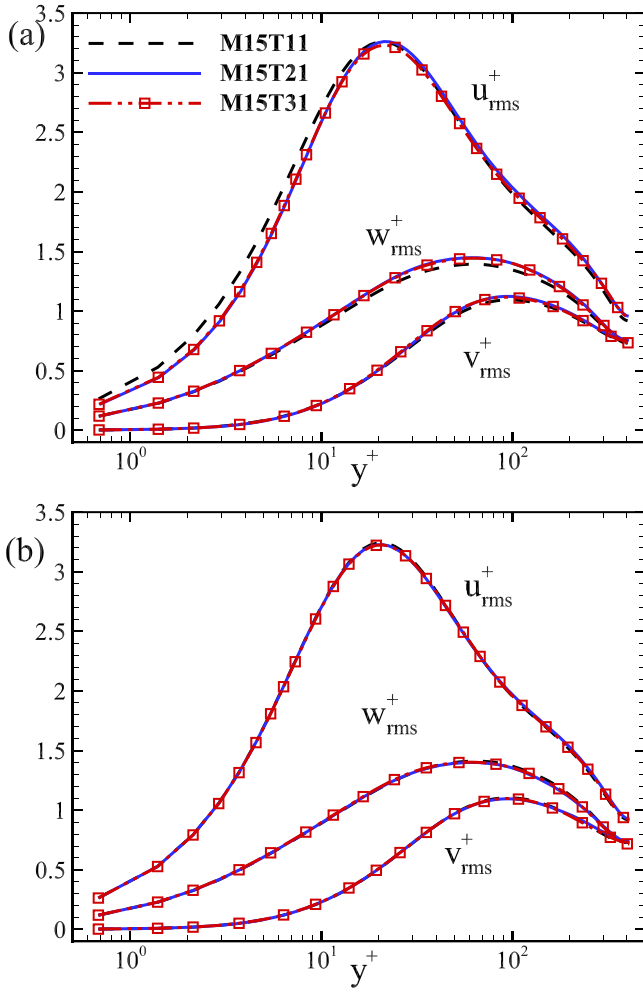


FIG. 3. Profiles of turbulence intensities from the three cases in (a) the bottom half and (b) the top half. Here, the rms values are normalized by u_τ .

case of M15T11 where the isothermal boundary condition is used at the bottom wall, T_{rms} is zero at the wall, and the local peak exists around $y^+ = 13$. For the cases of M15T21 and M15T31, T_{rms} 's are not zero at the wall but reach their maximum values. Furthermore, the values from M15T21 are larger than those from M15T31 in the bottom half of the channel. At $y^+ > 30$, T_{rms} from the three cases are relatively close. The obvious different behaviors near the bottom wall for the temperature fluctuations are consistent with those results observed in the incompressible case [18,20]. However, in their results, T_{rms} reached its maximum value at $y^+ \approx 15$ for the case with constant flux, whereas in the present compressible cases T_{rms} reached its maximum value at the wall. We also carried out three similar DNSs at $\text{Ma} = 0.5$ whereas keeping other setups unchanged. Although the magnitudes of T_{rms} are reduced (not shown here for brevity), its maximum value again locates at the wall for the cases with fixed $q_{w,b}$ or $T_{f,b}$. On the other hand, for the adiabatic walls in compressible turbulent boundary layers (see Fig. 12(a) Wenzel *et al.* [13] and Fig. 5(d) in Shadloo *et al.* [6]) and turbulent channel flows (see Tamano and Morinishi [5]), T_{rms} reaches its peak away from the wall. Therefore, we infer that the wall heat transfer may

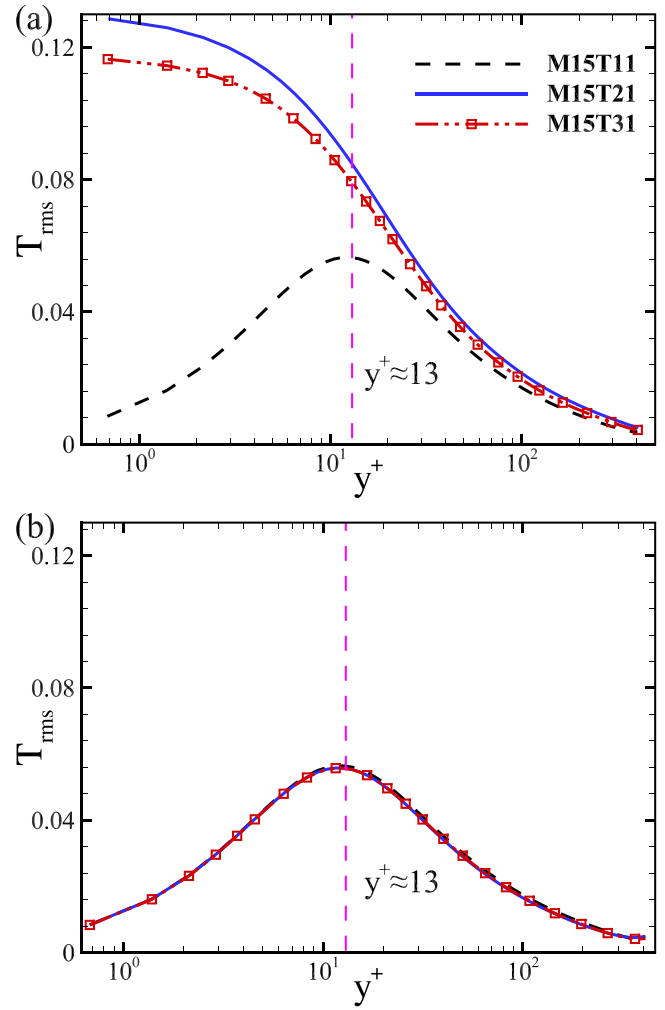


FIG. 4. Profiles of the rms values of the temperature fluctuations (normalized by T_{ref}) in (a) the bottom half and (b) the top half.

enhance the temperature fluctuations near the wall, which will result in the maximum of T_{rms} at the wall. Since the thermal boundary conditions are the same at the top wall for all three cases, and the basic statistics of velocity and temperature fields are almost the same on the top half, our discussions in the following will mainly be limited to the bottom half of the channel unless stated otherwise.

Figure 5 shows the profiles of $\langle u'v' \rangle$, $\langle u'T' \rangle$, and $\langle v'T' \rangle$ in the bottom half of the channel. Again, it is shown that there is no obvious difference between the cases of M15T21 and M15T31 for all three quantities and that some tiny deviations could be observed between the case of M15T11 and M15T21 for $\langle u'v' \rangle$ and $\langle v'T' \rangle$, whereas evident deviations can be observed between M15T11 and M15T21 for $\langle u'T' \rangle$ in the near-wall region with $y^+ \lesssim 30$. These results are in consistency with those results discussed before. It should be noted that, in incompressible flows with passive heat transfer, Tiselj *et al.* [23] and Flageul *et al.* [20] also observed profound effect on the statistics of the temperature fluctuations between the isoflux and the isothermal wall-boundary conditions in the near-wall region. However, the influence region of different boundary conditions was rather close to the wall with $y^+ < 10$

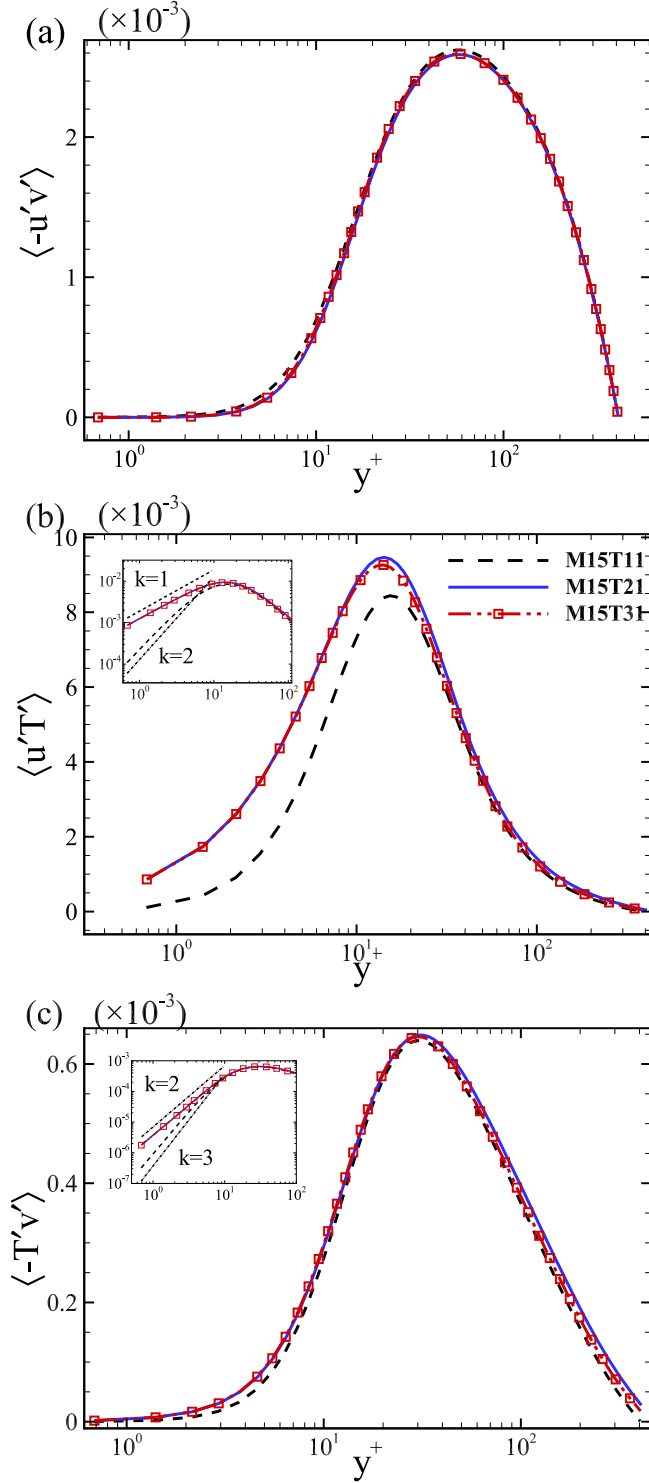


FIG. 5. Profiles of (a) $\langle u'v' \rangle$ (normalized by $u_m u_m$), (b) $\langle u'T' \rangle$ (normalized by $u_m T_{\text{ref}}$) and (c) $\langle v'T' \rangle$ (normalized by $u_m T_{\text{ref}}$) in the bottom half of the channel. Please note that they are zero for all cases at the wall. The near-wall asymptotic behaviors of $\langle u'T' \rangle$ and $\langle v'T' \rangle$ are also shown in the insets in (b) and (c).

for the incompressible case. We believe that the coupling of the thermal field and the velocity field extends the influence region of different thermal boundary conditions. According to the Taylor series expansions of the fluctuating velocity and

temperature at the wall [41], we may obtain the theoretical asymptotic behavior of $\overline{u'T'}$ and $\overline{v'T'}$, and they are shown in Table II. The second and third boundary conditions allow the temperature fluctuations at the wall, which will result in smaller scaling exponents in the near-wall region for $\langle v'T' \rangle$ and $\langle u'T' \rangle$ for M15T21 and M15T31 as compared to M15T11. This is confirmed by the insets in Figs. 5(b) and 5(c). It should be noted that the present wall-normal resolution cannot fully recover the near-wall behavior of $\langle v'T' \rangle$ within $y^+ \lesssim O(1)$ ($R1$ region) as reported by Baranwal *et al.* [41], who showed that the scaling exponent of $\langle v'T' \rangle$ in the $R1$ region with isothermal walls at $M_b = 1.5$ and $\text{Re}_b = 5752$ is around 2.2, a value close to the theoretical estimation for compressible flows. However, our result for M15T11 matches very well with theirs in the $R2$ region ($1.5 < y^+ < 7$) with the scaling exponent around 2.8.

B. Normalized probability density function of velocity and temperature fields

In the above, we have discussed the effect of different thermal boundary conditions by analyzing the low-order statistics of the velocity and temperature field. In order to further understand the influence of different boundary conditions on the velocity and temperature fields, the normalized probability density function (p.d.f.) will be analyzed here.

Figure 6 shows the normalized p.d.f.s of temperature fluctuations from different cases at different wall-normal locations away from both walls. It is obvious that, near the bottom wall where different thermal boundary conditions are used, there exist significant differences in the p.d.f.s of the temperature fluctuations between the cases of M15T11 and M15T21, whereas no obvious differences can be discerned between the cases of M15T21 and M15T31. On the top half of the channel where the same thermal boundary conditions are used, the p.d.f.s of temperature fluctuations from all three cases collapse with each other. This is also consistent with those results discussed above. At the location with $y^+ \approx 5$ away from the bottom wall [see Fig. 6(a)], the p.d.f. from the case of M15T11 is positive skewed, whereas those from the cases of M15T21 and M15T31 are negative skewed. It is interesting to note that the p.d.f. of fluctuating temperature in M15T11 behaves very similarly to that of the streamwise velocity fluctuations [see Fig. 7(a) $y^+ = 5$]. This can be explained by the fact of the no-slip boundary condition for velocity and the fixed temperature boundary condition in M15T11, and the fact of strong correlation between u' and T' (not shown here). Due to the constraints at the wall, the velocity fluctuations and temperature fluctuations near the wall are small in magnitude [see Figs. 3(a) and 4(a)] in M15T11. It is unlikely that a large negative velocity or temperature fluctuation will occur since there is no location in the flow that has a lower mean value of velocity or temperature than the wall (where $\bar{u} = 0$ and $\bar{T} = \bar{T}_{\text{min}}$). However, large positive fluctuations of u' or T' can easily occur when high-speed or high-temperature fluid away from the wall moves towards the wall. Nevertheless, for M15T21 and M15T31, the second and third boundary conditions will change the temperature fluctuations near the wall, and they become more coherent in the streamwise direction (see the later discussions in Sec. III C).

TABLE II. The asymptotic behavior of the turbulent heat flux.

Term	Incompressible case	M15T11	M15T21	M15T31
$\overline{u'T'}$	$\propto y^2 + O(y^3)$	$\propto y^2 + O(y^3)$	$\propto y + O(y^2)$	$\propto y + O(y^2)$
$\overline{v'T'}$	$\propto y^3 + O(y^4)$	$\propto y^2 + O(y^3)$ or $y^3 + O(y^4)$	$\propto y + O(y^2)$ or $y^2 + O(y^3)$	$\propto y + O(y^2)$ or $y^2 + O(y^3)$

The values of the temperature fluctuations are no longer small in magnitude as shown in Fig. 4(a). Therefore, large negative temperature fluctuations can also occur in the near-wall region. This may provide a clue to the negatively skewed p.d.f.s at $y^+ = 5$ in M15T21 and M15T31. When the location moves further away from the bottom wall to $y^+ \approx 15$ [see Fig. 6(b)], the p.d.f.s from the cases M15T21 and M15T31 are skewed more severely, whereas that from the case M15T11 approach them. The right leg is very close to those from the cases of M15T21 and M15T31, whereas its left leg has much lower values. When the location further moves away from the bottom wall [see Fig. 6(c)], the p.d.f.s from the three cases begin to collapse with each other except some scattering at $T'/T_{\text{rms}} > 2$.

Figure 7 shows the normalized p.d.f.s of the streamwise velocity fluctuation u' and the wall-normal velocity fluctuation

v' at several wall-normal locations. It is seen that, at all the four chosen locations, the p.d.f.s from the cases with different thermal boundary conditions collapse with each other for both u' and v' , although we have shown in Fig. 3(a) that some differences can be observed for the rms values of u' near the bottom wall. We also investigate the p.d.f.s of pressure and density fluctuations. The results show (not shown here for brevity) that the p.d.f.s of density fluctuations have similar performance to the temperature fluctuations from the three cases, whereas the p.d.f.s of pressure fluctuations behave more likely to those of the velocity fluctuations. Combining the basic statistics and the p.d.f.s of the temperature and velocity fields discussed above, we believe that in compressible channel flow different wall thermal boundary conditions will affect the temperature field, but the influence will be limited only in the near-wall region. At the same time, the influence on the

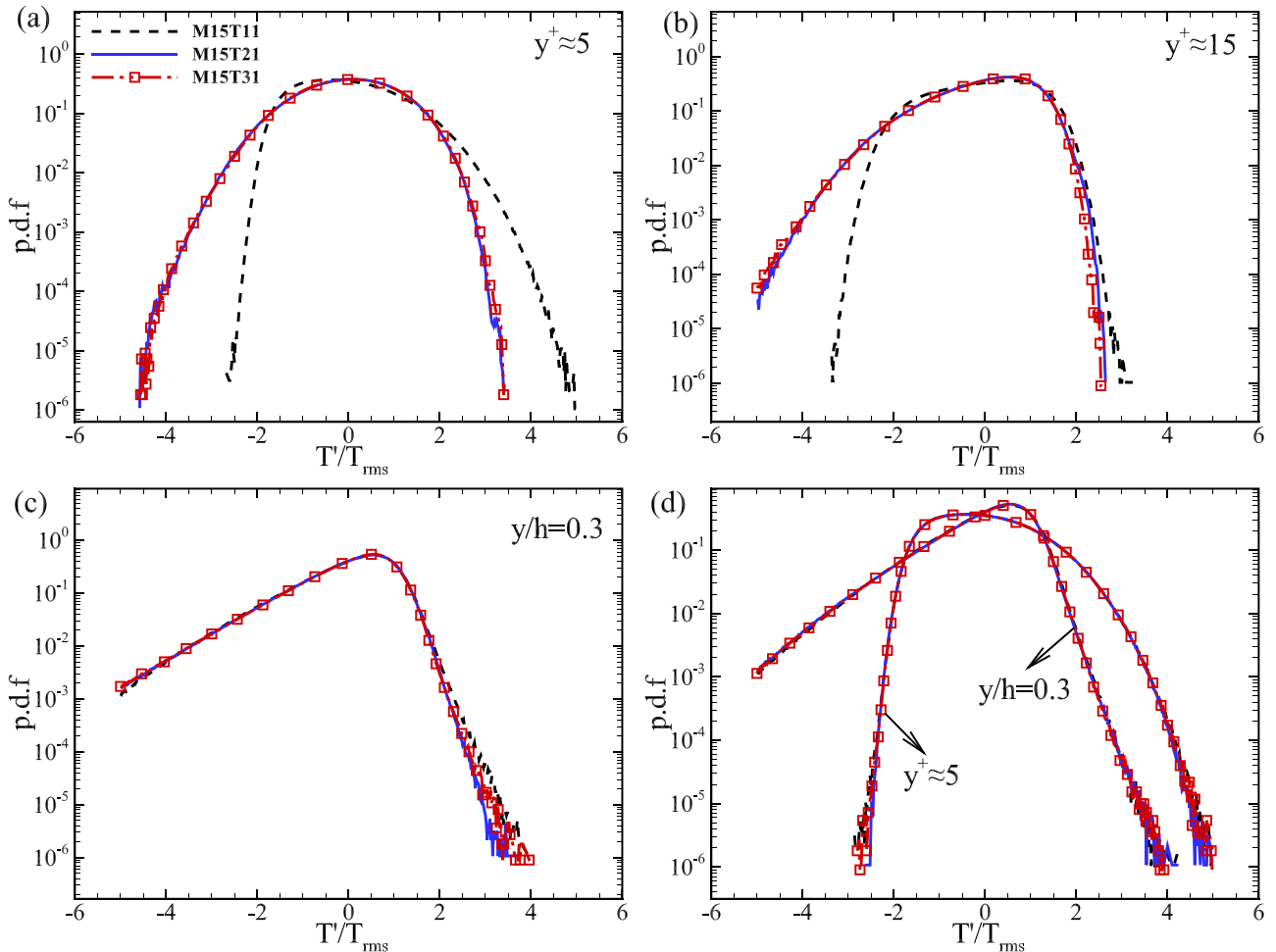


FIG. 6. Normalized p.d.f.s of the temperature fluctuations from different cases at different wall-normal locations. (a) $y^+ \approx 5$, (b) $y^+ \approx 15$, (c) $y/h = 0.3$ from the bottom wall, and (d) $y^+ \approx 5$ and $y/h = 0.3$ from the top wall.

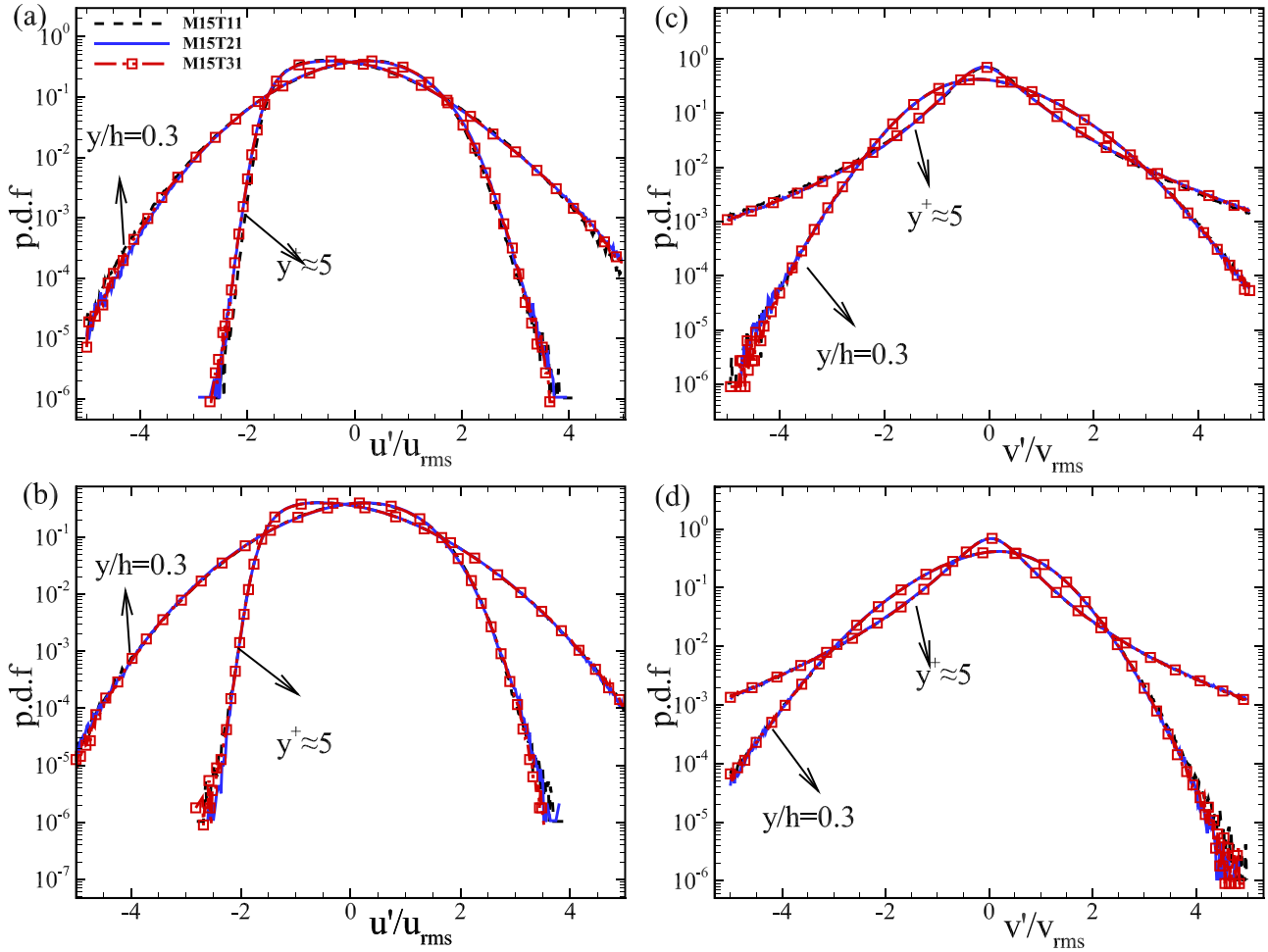


FIG. 7. Normalized p.d.f.s of the streamwise velocity fluctuations (a) and (b) and wall-normal velocity fluctuations (c) and (d) at different wall-normal locations. Here, (a) and (c) are in the bottom half and (b) and (d) are in the top half.

velocity field is almost negligible, whether in the near-wall region or in the region far away from the wall, which is quite similar to those observed in incompressible cases where the temperature field is a passive scalar.

C. Temperature stripes near the wall

Now, we would like to investigate the temperature stripes structures in the near-wall region near the bottom wall. Differently from the isothermal boundary condition at the bottom wall, the isoflux and the Robin boundary conditions allow the temperature differences on the wall, and this argument could be verified by Fig. 8 where the temperature fluctuation contours at the bottom wall from the cases of M15T21 and M15T31 are shown. Clearly, many high-low temperature stripes present at the bottom wall for the two cases, which indicates the thermal structures on the wall. Away from the wall, the high-low temperature stripes exist for all three cases, and we show in Fig. 9 the snapshots of the temperature fluctuation at $y^+ \approx 15$ away from the bottom wall. For the case of M15T11, very few extreme events on the temperature fluctuations with $|T'/T_{ref}| > 0.1$ are observed, whereas for the cases of M15T21 and M15T31, more extreme events are observed, which is consistent with their larger T_{rms}/T_{ref} values

as shown in Fig. 4(a). Furthermore, the stripes from the cases of M15T21 and M15T31 are much longer than those from the case of M15T11.

In order to quantitatively measure the temperature stripes' spacing and length following the procedure

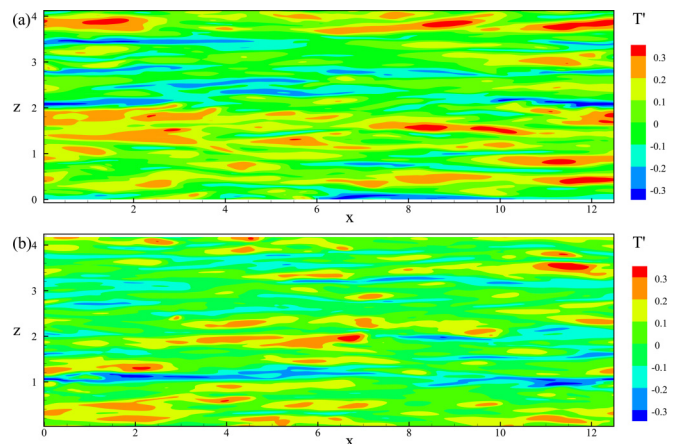


FIG. 8. The instantaneous temperature contours T'/T_{ref} at the bottom wall from the cases of (a) M15T21 and (b) M15T31.

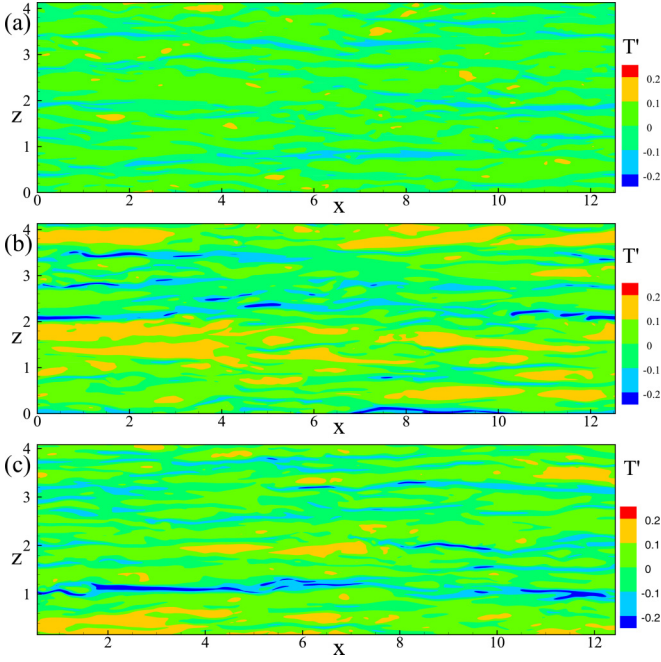


FIG. 9. The instantaneous temperature contours T'/T_{ref} at $y^+ \approx 15$ away from the bottom wall from the cases of (a) M15T11, (b) M15T21, and (c) M15T31.

applied to the velocity stripes [1], the two-point correlation function will be used. The correlation function of quantity ϕ in the homogeneous z direction is defined as

$$R_{\phi\phi}(r_z; y) = \frac{\overline{\phi'(x, y, z, t)\phi'(x, y, z + r_z, t)}}{\overline{\phi'(x, y, z, t)\phi'(x, y, z, t)}}. \quad (8)$$

The two-point correlation function in the homogeneous x direction can be defined similarly.

Figure 10 shows the spanwise and streamwise two-point correlations for the temperature at $y^+ \approx 15$ away from the bottom wall for the three cases. For the temperature's spanwise two-point correlations as shown in Fig. 10(a), they behave very similarly. That is, they decay fast until their minimal values and then oscillate around zero, which is consistent with those figures shown in Coleman *et al.* [2]. Nevertheless, the points at which the minimal values arrive are different, and they are around $z/h = 0.2, 0.3,$ and 0.28 for the cases M15T11, M15M21, and M15T31, respectively. Therefore, the mean spacing among the stripes are different for the three cases, and it is about 80 wall units for the case of M15T11, and about 120 wall units for the cases of M15T21 and M15T31, which indicates that the second and third kinds of thermal boundary conditions can increase the mean temperature stripes spacing near the bottom wall. For the temperature's streamwise two-point correlations as shown in Fig. 10(b), an obvious difference can be observed. Although they decay with x , they are not zero for the cases of M15T21 and M15T31 even when $x/h = L_x/2$, whereas it is zero for the case of M15T11 at $x/h \geq 5$. We attribute the different behaviors of the streamwise two-point correlations among the case of M15T11 and the cases of M15T21 and M15T31 to

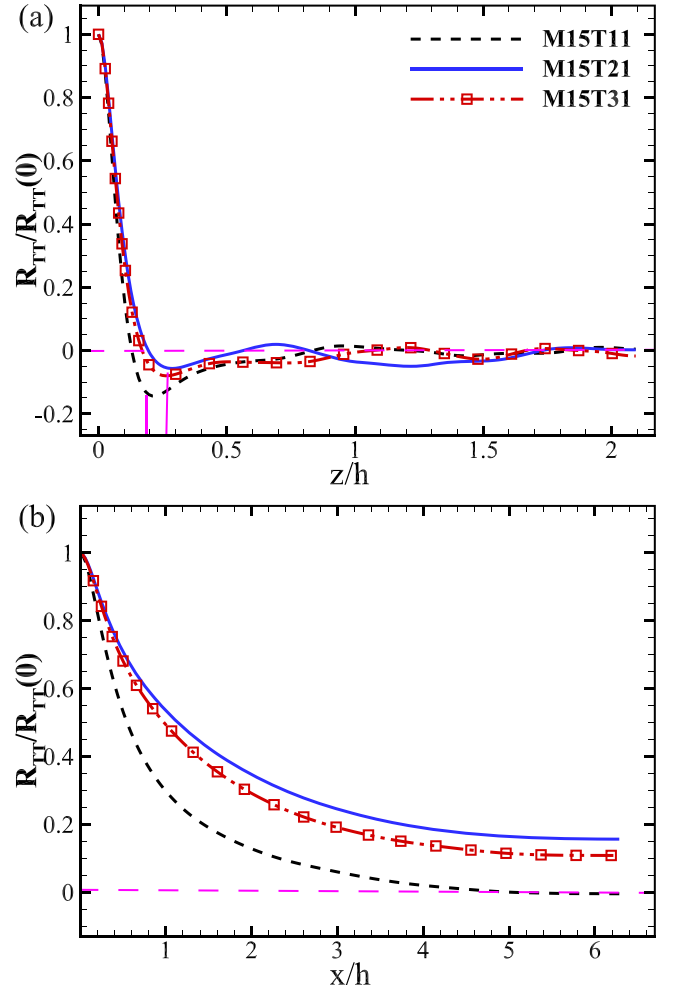


FIG. 10. (a) Spanwise and (b) streamwise two-point correlations for the temperature at $y^+ \approx 15$ away from the bottom wall for the three cases.

different thermal boundary conditions. For the case of M15T11, no temperature stripe is allowed on the wall due to the isothermal boundary condition. On the other hand, the stripes existed on the wall for the cases of M15T21 and M15T31, and they can be more stable and longer in the near-wall region.

In Tiselj *et al.* [18], they also reported R_{TT} will persist nonzero even for a doubled streamwise computational domain ($L_x = 10\pi h$) in an incompressible channel with passive scalar at $\text{Pr} = 0.71$ and claimed that R_{TT} did not show any differences larger than the statistical uncertainty in a longer domain. We also performed three extra simulations with $L_x = 10\pi h$, and our results indeed show that R_{TT} will decay to zero at $x/h \geq 10$ for the case of M15T21 and case of M15T31 (not shown), indicating that there are much longer streamwise temperature stripes in the near-wall region in M15T21 and M15T31. As compared to the results in M15T11, it is evident that the second and third thermal boundary conditions can elongate the temperature stripes in the near-wall region, which is consistent with those contours shown in Fig. 9. It should be noted that most of the single-point statistics do not show

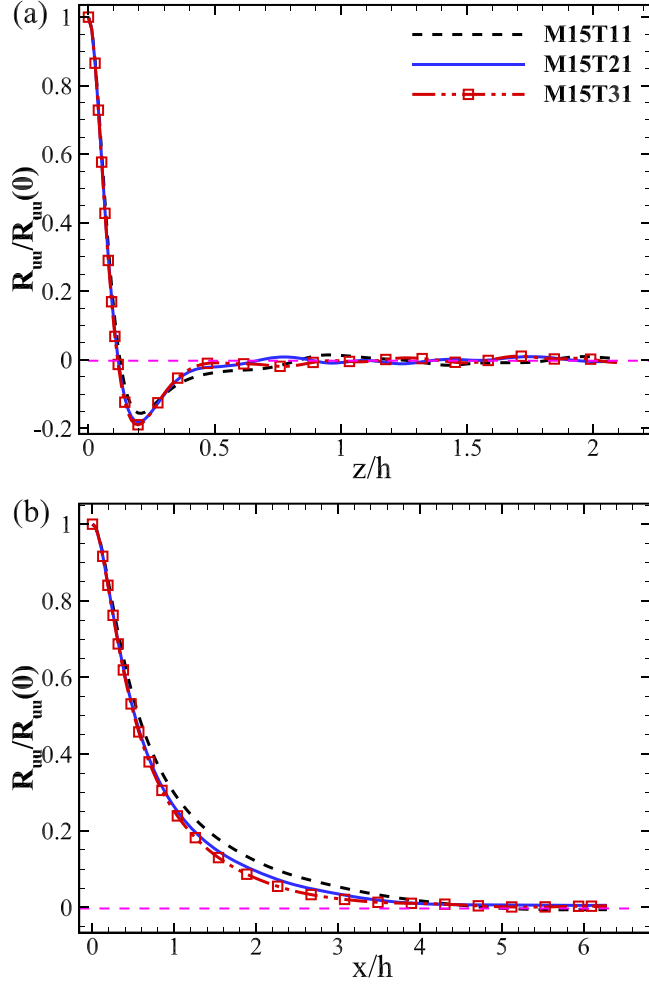


FIG. 11. (a) Spanwise and (b) streamwise two-point correlations for the streamwise velocity component at $y^+ \approx 15$ away from the bottom wall for the three cases.

obvious difference for the simulations with different L_x 's (not shown).

Figure 11 shows the spanwise and streamwise two-point correlations for the streamwise velocity component at $y^+ \approx 15$ away from the bottom wall from all three cases. It is evident that no clear deviation exists among the three cases for both the spanwise and the streamwise two-point correlations. They all reach their minimal values around $z/h = 0.2$ for the spanwise R_{uu} and decay to zero at $x/h \geq 4$ for the streamwise R_{uu} . Again, the different thermal boundary conditions will have no obvious impact on the velocity stripes.

D. Budget of the internal energy

We would like to investigate the budget of the mean internal energy to understand the effect of different thermal boundary conditions on the temperature fields. The budget of mean internal energy equation for fully developed turbulent channel flow [3,5] is

$$\underbrace{D_{em1} + D_{em2}}_{D_{em}} + \varepsilon_{em} + \varepsilon_k + P_{em} + C_k = 0, \quad (9)$$

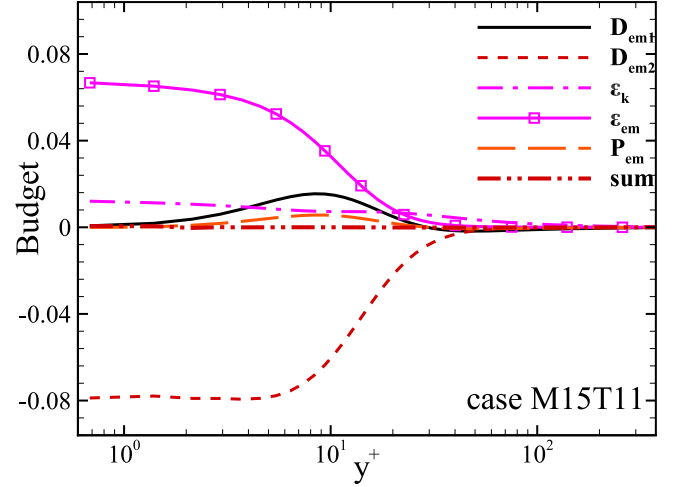


FIG. 12. Budget of the mean internal equation for case of M15T11 in the bottom half of the channel. $C_k \approx 0$ is not shown. The terms are normalized by $\rho_m u_m^3/h$.

where $D_{em1} = -\partial(C_v \overline{\rho v'' T''})/\partial y$ and $D_{em2} = -\partial \overline{q_2}/\partial y$ are the turbulent diffusion term and the molecular diffusion term, respectively. (The summation $D_{em} = D_{em1} + D_{em2}$ is the total diffusion term). $\varepsilon_{em} = \overline{\tau_{i2} \partial \bar{u}_i / \partial y}$ is the mean-flow dissipation, $\varepsilon_k = \overline{\tau'_{ij} \partial u'_j / \partial x_j}$ is the turbulent dissipation, $P_{em} = -\overline{p' \partial \bar{v} / \partial y}$ is the mean-flow pressure work, and $C_k = -\overline{p' \partial u'_j / \partial x_j}$ is the fluctuation pressure dilatation (fluctuation pressure work), respectively. As pointed out by Huang *et al.*[3], terms ε_{em} and ε_k are irreversible terms which transfer the energy from the mean kinetic energy and turbulent kinetic energy to the mean internal energy, whereas the C_k term is an additional compressibility term due to the pressure fluctuations, which can exchange energy between the mean internal energy and the turbulent kinetic energy.

Figure 12 shows the mean internal energy budget terms (normalized by $\rho_m u_m^3/h$) in the bottom half channel for case of M15T11. The fluctuation pressure work term C_k is almost zero in the whole channel, and it is not shown in the figure. The summation of all terms is zero, which also confirms that the case has reached its fully developed state. It is seen that the molecular diffusion D_{em2} and the mean-flow dissipation ε_{em} dominate near the wall. This indicates that the main contribution to the mean internal energy in the near-wall region is the transfer from the mean kinetic energy, which is mainly balanced by the molecular diffusion term. The results are also consistent with the previous results [5].

To display the effect of different thermal boundary conditions on the budget terms of the mean internal energy, Fig. 13 shows D_{em1} , D_{em2} , ε_{em} , ε_k , and P_{em} at the bottom half of the channel for all three cases. It is seen again that all the terms from M15T21 and M15T31 collapse very well in the bottom half of the channel, whereas some deviations can be seen in the near-wall region (within $y^+ < 15$) between M15T11 and M15T21. This result is consistent with those results discussed above, although the influence region is smaller than that for the temperature fluctuations.

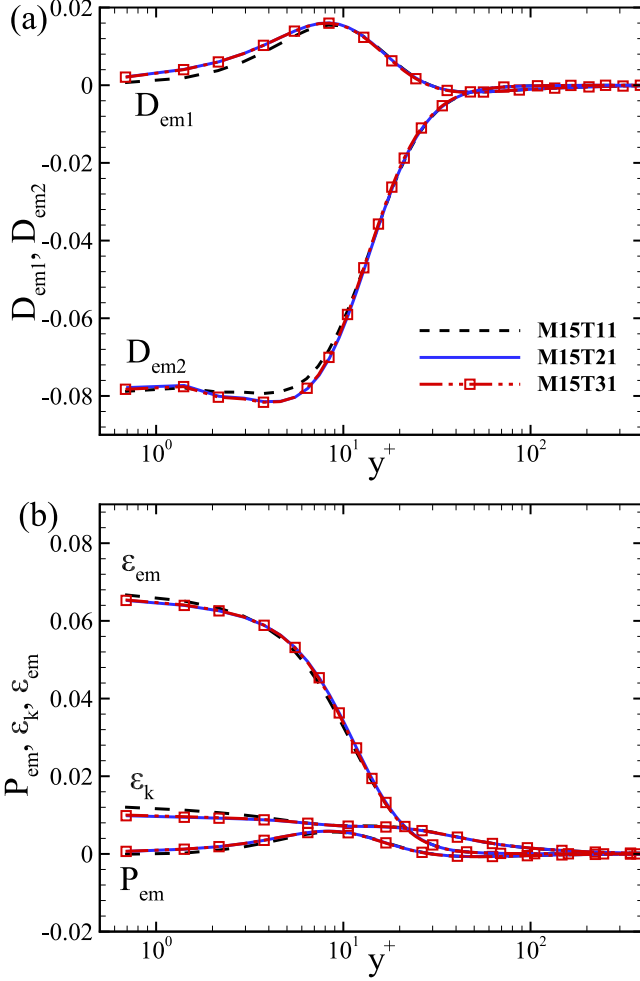


FIG. 13. Budget terms for all three cases in the bottom half of the channel: (a) D_{em1} and D_{em2} ; (b) ε_{em} , ε_k , and P_{em} . The terms are normalized by $\rho_m u_m^3 / h$.

E. Budget of the temperature variance

At last, the transport equation of temperature variance is investigated, and the equation is [5]

$$P_{TV} + C_{TV1} + C_{TV2} + C_{TV3} + D_{TV1} + D_{TV2} + \varepsilon_{TV} = 0, \quad (10)$$

where the production term P_{TV} , compressibility terms C_{TV1} , C_{TV2} , and C_{TV3} , turbulent diffusion term D_{TV1} , molecular diffusion term D_{TV2} , and dissipation per unit volume ε_{TV} are defined as follows:

$$P_{TV} = -\langle \rho \rangle \{ T'' u_2'' \} \frac{\partial \langle T \rangle}{\partial x_2}, \quad (11)$$

$$C_{TV1} = -\frac{1}{c_v} \left[\langle T'' \rangle \langle p \rangle \frac{\partial \langle u_2 \rangle}{\partial x_2} + \left\langle T'' p' \frac{\partial u_i'}{\partial x_i} \right\rangle + \langle T' p' \rangle \frac{\partial \langle u_2 \rangle}{\partial x_2} + \langle p \rangle \left\langle T' \frac{\partial u_i'}{\partial x_i} \right\rangle \right], \quad (12)$$

$$C_{TV2} = \frac{1}{c_v} \left[\langle T'' \rangle \langle \tau_{ij} \rangle \frac{\partial \langle u_i \rangle}{\partial x_2} + \left\langle T'' \tau'_{ij} \frac{\partial u_i'}{\partial x_j} \right\rangle \right]$$

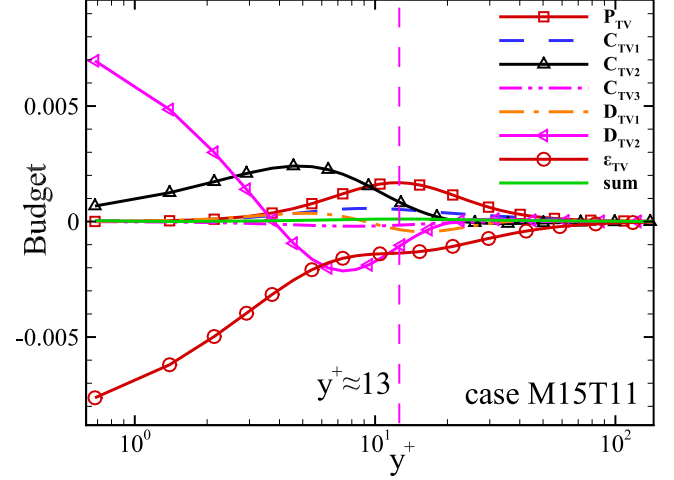


FIG. 14. Profiles of the budget terms in M15T11 (normalized by $\rho_m u_m T_{ref}^2 / h$).

$$+ \langle T' \tau'_{ij} \rangle \frac{\partial \langle u_i \rangle}{\partial x_2} + \langle \tau_{ij} \rangle \left\langle T' \frac{\partial u_i'}{\partial x_j} \right\rangle \right], \quad (13)$$

$$C_{TV3} = -\frac{1}{c_v} \langle T'' \rangle \frac{\partial \langle q_2 \rangle}{\partial x_2}, \quad (14)$$

$$D_{TV1} = -\frac{1}{2} \frac{\partial \langle (\rho) \{ T''^2 u_2'' \} \rangle}{\partial x_2}, \quad (15)$$

$$D_{TV2} = \frac{1}{c_v} \frac{\partial}{\partial x_2} \left(\langle T' \kappa' \rangle \frac{\partial \langle T \rangle}{\partial x_2} + \left\langle T' \kappa' \frac{\partial T'}{\partial x_2} \right\rangle + \langle \kappa \rangle \left\langle T' \frac{\partial T'}{\partial x_2} \right\rangle \right), \quad (16)$$

$$\varepsilon_{TV} = -\frac{1}{c_v} \left[\left\langle \kappa' \frac{\partial T'}{\partial x_2} \right\rangle \frac{\partial \langle T \rangle}{\partial x_2} + \left\langle \kappa' \frac{\partial T'}{\partial x_j} \frac{\partial T'}{\partial x_j} \right\rangle + \langle \kappa \rangle \left\langle \frac{\partial T'}{\partial x_j} \frac{\partial T'}{\partial x_j} \right\rangle \right]. \quad (17)$$

Figure 14 shows the transport budget terms in the bottom half channel for M15T11. It is found that P_{TV} , C_{TV2} , D_{TV2} , and ε_{TV} are the dominated terms, and the main balance in the near-wall region is between D_{TV2} and ε_{TV} . The summation of all terms is very close to zero, demonstrating the correctness of our statistics. Figure 15 shows the four dominated terms in the bottom half of the channel for all three cases. It is seen that C_{TV2} , D_{TV2} , and ε_{TV} exhibit differently between M15T11 and M15T21 (or M15T31) in the near-wall region, whereas there is no substantial change in P_{TV} among the three cases. C_{TV2} has the largest positive value in the near-wall region, which will be balanced by the summation of D_{TV2} and ε_{TV} . Furthermore, C_{TV2} from all three cases behave similarly as T_{rms} shown in Fig. 4(a), which might suggest that the compressibility term C_{TV2} is the main reason for a maximum T_{rms} at the wall for M15T21 and M15T31.

IV. CONCLUSIONS

We have carried out DNSs of fully developed compressible channel flows to investigate the equivalence of different thermal boundary conditions at fixed $Re = 6000$, $Ma = 1.5$. Three different thermal boundary conditions are adopted at the bottom wall, including the first boundary condition

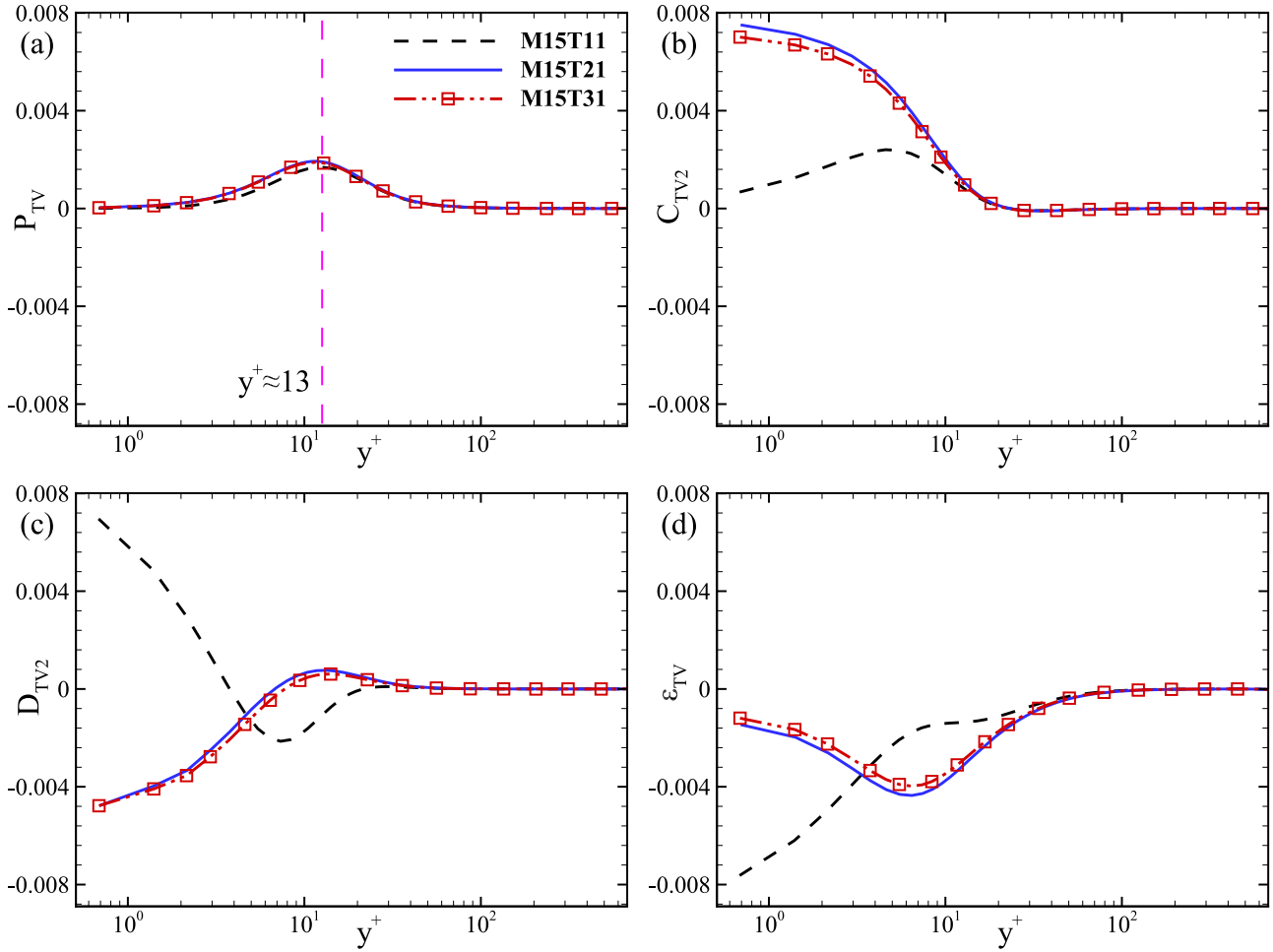


FIG. 15. Near-wall behavior of the dominated terms: (a) P_{TV} , (b) C_{TV2} , (c) D_{TV2} , and (d) ϵ_{TV} for all three cases.

with fixed wall temperature T_w (constant Dirichlet boundary condition), the second boundary condition with fixed wall heat-flux q_w (constant Neumann boundary condition), and the third boundary condition (Robin boundary condition). Here, the values of q_w and $T_{f,b}$ are chosen according to the results obtained in the isothermal cases to make sure that the three cases are almost the same. The turbulence statistics of the temperature and velocity fields, including mean profiles, rms values, second-order statistics, normalized probability density functions, and temperature stripes structures near the wall, and the budgets of internal energy and temperature variance are analyzed and compared, and the following main conclusions related to the equivalence of different thermal boundary conditions can be drawn:

(1) Different thermal boundary conditions will have an obvious impact on the temperature field in the near-wall region about $y^+ < 30$, and the influence is negligible further away from the wall. The Neumann and Robin temperature boundary conditions allow the temperature fluctuations at the wall, making the temperature stripes more coherent in the streamwise direction with a larger spanwise spacing. Compared with those results in incompressible cases, the coupling between the temperature and the velocity indeed enlarges the influence region of different thermal boundary conditions.

(2) Although the velocity is coupled with temperature in compressible cases, the different thermal boundary conditions have negligible effect on the velocity field. Therefore, the simplest isothermal boundary conditions can be selected for the future study of velocity field in compressible wall-bounded flows.

(3) The statistics from the second and third thermal boundary conditions are very close, enabling to use the second boundary condition to mimic the more complex third boundary conditions.

(4) If the temperature fluctuations in the near-wall region are not the main concern, the isothermal boundary condition can also be used to mimic the second and third boundary conditions, which directly confirms the rationality of using the isothermal wall with recovery temperature T_r to replace the real adiabatic condition in the researches of compressible boundary layer.

The present paper provides direct numerical evidences on the equivalence and differences among three canonical thermal boundary conditions in compressible turbulent channel flows, which can be used to guide the community on choosing the appropriate thermal boundary condition. In the future, we will consider the solid-gas coupled thermal boundary conditions and investigate whether the flow field will be affected by solid heat conduction.

ACKNOWLEDGMENTS

We would like to thank Prof. X. Li for using his OPENCFD code. We would also like to acknowledge support by the National Natural Science Foundation of China (NSFC Grants

No. 92152101, No. 11822208, No. 92152301, and No. 91852205) and Guangdong provincial Key Laboratory (Grant No. 2019B121203001).

The authors report no conflict of interest.

-
- [1] L. Duan, I. Beekman, and M. P. Martin, Direct numerical simulation of hypersonic turbulent boundary layers. part 2. effect of wall temperature, *J. Fluid Mech.* **655**, 419 (2010).
- [2] G.N. Coleman, J. Kim, and R.D Moser, Numerical study of turbulent supersonic isothermal-wall channel flow, *J. Fluid Mech.* **305**, 159 (1995).
- [3] P. G. Huang, G. N. Coleman, and P. Bradshaw, Compressible turbulent channel flows: DNS results and modelling, *J. Fluid Mech.* **305**, 185 (1995).
- [4] Y. Morinishi, S. Tamano, and K. Nakabayashi, Direct numerical simulation of compressible turbulent channel flow between adiabatic and isothermal walls, *J. Fluid Mech.* **502**, 273 (2004).
- [5] S. Tamano and Y. Morinishi, Effect of different thermal wall boundary conditions on compressible turbulent channel flow at $M = 1.5$, *J. Fluid Mech.* **548**, 361 (2006).
- [6] M.S. Shadloo, A. Hadjadj, and F. Hussain, Statistical behavior of supersonic turbulent boundary layers with heat transfer at $M_\infty = 2$, *Int. J. Heat Fluid Flow* **53**, 113 (2015).
- [7] H. Foysi, S. Sarkar, and R. Friedrich, Compressibility effects and turbulence scalings in supersonic channel flow, *J. Fluid Mech.* **509**, 207 (2004).
- [8] A. Trettel and J. Larsson, Mean velocity scaling for compressible wall turbulence with heat transfer, *Phys. Fluids* **28**, 026102 (2016).
- [9] D. Modesti and S. Pirozzoli, Reynolds and Mach number effects in compressible turbulent channel flow, *Int. J. Heat Fluid Flow* **59**, 33 (2016).
- [10] M. Yu, C.X. Xu, and S. Pirozzoli, Genuine compressibility effects in wall-bounded turbulence, *Phys. Rev. Fluids* **4**, 123402 (2019).
- [11] M.S. Shadloo, A. Hadjadj, and F. Hussain, Temperature-invariant scaling for compressible turbulent boundary layers with wall heat transfer, *Heat Transfer Eng.* **39**, 923 (2018).
- [12] X. Yang, J. Urzay, S. Bose, and P. Moin, Aerodynamic heating in wall-modeled large-eddy simulation of high-speed flows, *AIAA J.* **56**, 731 (2018).
- [13] C. Wenzel, B. Selent, M. Kloker, and U. Rist, DNS of compressible turbulent boundary layers and assessment of data/scaling-law quality, *J. Fluid Mech.* **842**, 428 (2018).
- [14] M. M. Rai, T. B. Gatski, and G. Erlebacher, Direct simulation of spatially evolving compressible turbulent boundary layers, in *33rd Aerospace Sciences Meeting and Exhibit* (AIAA, Reston, VA, 1995), paper AIAA 95-0583.
- [15] S. Pirozzoli, F. Grasso, and T. B. Gatski, Direct numerical simulation and analysis of a spatially evolving supersonic turbulent boundary layer at $M=2.25$, *Phys. Fluids* **16**, 530 (2004).
- [16] L. Duan, I. Beekman, and M. P. Martin, Direct numerical simulation of hypersonic turbulent boundary layers. Part 3. Effect of Mach number, *J. Fluid Mech.* **672**, 245 (2011).
- [17] Y-B. Chu, Y-Q. Zhuang, and X-Y. Lu, Effect of wall temperature on hypersonic turbulent boundary layer, *J. Turbul.* **14**, 37 (2013).
- [18] I. Tiselj, R. Bergant, B. Mavko, I. Bajsic, and G. Hetsroni, Direct numerical simulation of turbulent heat transfer in channel flow with heat conduction in the solid wall, *J. Heat Transfer* **123**, 849 (2001).
- [19] E. Pazera, Heat transfer in periodically laminated structures—third type boundary conditions, *Int. J. Comput. Methods Eng. Sci. Mech.* **18**, 2041011 (2021).
- [20] C. Flageul, S. Benhamadouche, E. Lamballais, and D. Laurence, DNS of turbulent channel flow with conjugate heat transfer: Effect of thermal boundary conditions on the second moments and budgets, *Int. J. Heat Fluid Flow* **55**, 34 (2015).
- [21] N. Kasagi, Y. Tomita, and A. Kuroda, Direct numerical simulation of passive scalar field in a turbulent channel flow, *J. Heat Transfer* **114**, 598 (1992).
- [22] H. Kawamura, H. Abe, and Y. Matsuo, DNS of turbulent heat transfer in channel flow with respect to Reynolds and Prandtl number effects, *Int. J. Heat Fluid Flow* **20**, 196 (1999).
- [23] I. Tiselj, E. Pogrebnyak, C. Li, A. Mosyak, and G. Hetsroni, Effect of wall boundary condition on scalar transfer in a fully developed turbulent flume, *Phys. Fluids* **13**, 1028 (2001).
- [24] Y. Seki, H. Abe, and H. Kawamura, Comparison of scalar turbulence quantities through DNS of turbulent heat transfer in a channel flow with different thermal boundary conditions, *Nippon Kikai Gakkai Ronbunshu, B-hen* **70**, 2089 (2004).
- [25] S. Pirozzoli, M. Bernardini, and P. Orlandi, Passive scalars in turbulent channel flow at high Reynolds number, *J. Fluid Mech.* **788**, 614 (2016).
- [26] J. M. Avellaneda, F. Bataille, and A. Toutant, DNS of turbulent low Mach channel flow under asymmetric high temperature gradient: Effect of thermal boundary condition on turbulence statistics, *Int. J. Heat Fluid Flow* **77**, 40 (2019).
- [27] F. Alcántara-Ávila, S. Hoyas, and M. J. Perez-Quiles, DNS of thermal channel flow up to $Re_\tau = 2000$ for medium to low Prandtl numbers, *Int. J. Heat Mass Transf.* **127**, 349 (2018).
- [28] Francisco Alcántara-Ávila, S. Hoyas, and M. J. Perez-Quiles, Direct numerical simulation of thermal channel flow for $Re_\tau = 5000$ and $Pr = 0.71$, *J. Fluid Mech.* **916**, A29 (2021).
- [29] S. Serra, A. Toutant, F. Bataille, and Y. Zhou, High-temperature gradient effect on a turbulent channel flow using thermal large-eddy simulation in physical and spectral spaces, *J. Turbul.* **13**, N49 (2012).
- [30] A. Toutant and F. Bataille, Turbulence statistics in a fully developed channel flow submitted to a high temperature gradient, *Int. J. Therm. Sci.* **74**, 104 (2013).
- [31] D. Dupuy, A. Toutant, and F. Bataille, Turbulence kinetic energy exchanges in flows with highly variable fluid properties, *J. Fluid Mech.* **834**, 5 (2018).
- [32] G. Mangeon, S. Benhamadouche, J.-F. Wald, and R. Manceau, Extension to various thermal boundary conditions of the elliptic blending model for the turbulent heat flux and the temperature variance, *J. Fluid Mech.* **905**, A1 (2020).

- [33] W. Sutherland, The viscosity of gases and molecular force, *Philos. Mag.* **36**, 507 (1893).
- [34] X. Liang and X.L. Li, DNS of a spatially evolving hypersonic turbulent boundary layer at Mach 8, *Sci. China: Phys., Mech. Astron.* **56**, 1408 (2013).
- [35] X. Liang and X.L. Li, Direct numerical simulation on Mach number and wall temperature effects in the turbulent flows of flat-plate boundary layer, *Commun. Comput. Phys.* **17**, 189 (2015).
- [36] X.P. Chen, X. L. Li, and Z.C. Zhu, Effects of dimensional wall temperature on velocity-temperature correlations in supersonic turbulent channel flow of thermally perfect gas, *Sci. China: Phys., Mech. Astron.* **62**, 64711 (2019).
- [37] X. Li, F-L. Tong, C-P. Yu, and X-L. Li, Statistical analysis of temperature distribution on vortex surfaces in hypersonic turbulent boundary layer, *Phys. Fluids* **31**, 106101 (2019).
- [38] P. Zhang and Z. Xia, Contribution of viscous stress work to wall heat flux in compressible turbulent channel flows, *Phys. Rev. E* **102**, 043107 (2020).
- [39] W.P. Li, Y.T. Fan, D. Modesti, and C. Cheng, Decomposition of the mean skin-friction drag in compressible turbulent channel flows, *J. Fluid Mech.* **875**, 101 (2019).
- [40] X.P. Chen and F. Fei, Effects of dimensional wall temperature on reynolds stress budgets in a supersonic turbulent channel flow with thermally perfect gas, *Int. J. Comput. Fluid Dyn.* **32**, 315 (2018).
- [41] A. Baranwal, D. A. Donzis, and R. D. W. Bowersox, Asymptotic behaviour at the wall in compressible turbulent channels, *J. Fluid Mech.* **933**, A28 (2022).